

The distribution of two-dimensional eccentricity of Sunyaev-Zeldovich Effect and X-ray surface brightness profiles

Y.-G. Wang and Z.-H. Fan

Department of Astronomy, Peking University, Beijing 100871, China

wangyg@bac.pku.edu.cn, fan@bac.pku.edu.cn

ABSTRACT

With the triaxial density profile of dark matter halos and the corresponding equilibrium gas distribution, we derive two-dimensional Sunyaev-Zeldovich (SZ) effect and X-ray surface brightness profiles for clusters of galaxies. It is found that the contour map of these observables can be well approximated by a series of concentric ellipses with scale-dependent eccentricities. The statistical distribution of their eccentricities (or equivalently axial ratios) is analyzed by taking into account the orientation of clusters with respect to the line of sight and the distribution of the axial ratios and the concentration parameters of dark matter halos. For clusters of mass $10^{13}h^{-1}M_{\odot}$ at redshift $z = 0$, the axial ratio is peaked at $\eta \sim 0.9$ for both SZ and X-ray profiles. For larger clusters, the deviation from circular distributions is more apparent, with η peaked at $\eta \sim 0.85$ for $M = 10^{15}h^{-1}M_{\odot}$. To be more close to observations, we further study the axial-ratio distribution for mass-limited cluster samples with the number distribution of clusters at different redshifts described by a modified Press-Schechter model. For a mass limit of value $M_{lim} = 10^{14}h^{-1}M_{\odot}$, the average axial ratio is $\langle \eta \rangle \sim 0.84$ with a tail extended to $\eta \sim 0.6$. With fast advance of high quality imaging observations of both SZ effect and X-ray emissions, our analyses provide a useful way to probe cluster halo profiles and therefore to test theoretical halo-formation models.

Subject headings: cosmology: theory— galaxy: cluster — large-scale structure of universe

1. Introduction

Following abundant observations of various kinds, a concordance cosmological model has emerged (e.g., Spergel et al. 2003). The geometry of the universe is nearly flat with

the total density of the universe Ω_{tot} very close to unity. Among which, about 70% is in the form of dark energy with negative pressure, and about 25% is composed of non-baryonic dark matter. The familiar baryonic matter contributes only about 5% of the total matter density in the universe. It is apparent that dark matter plays dominant roles in the structure formation.

Besides large-scale structures, it is of great cosmological interest to understand the properties of individual dark matter halos. Extensive studies with high resolution simulations have been performed in this aspect (e.g., Fukushige & Makino 1997, 2001; Moore et al. 1998; Jing 2000; Jing & Suto 2000). Navarro, Frenk and White (1996, 1997) put forward a universal density profile (NFW profile) to describe the spherical mass distribution of dark matter halos of different masses. Confronted with observations, the validity of the profile has been tested for dwarf galaxies, galaxies, as well as clusters of galaxies. Certain degree of disagreement between the inferred inner profile from some observations and the NFW one raised a potential small-scale problem for cold dark matter models. Despite that, the NFW profile has been applied widely in different studies (e.g., Bartelmann et al. 2001; Li & Ostriker 2002; Wyithe et al. 2001). However, the sphericity assumed in the NFW profile is clearly an approximation, and could introduce systematic errors in theoretical predictions, and further in cosmological parameter extractions from observations (e.g., Birkinshaw 1999). Among others (Dubinski 1994; Jing, et al. 1995; Thomas et al. 1998; Yoshida et al. 2000; Meneghetti et al. 2001), Jing and Suto (2002) did detailed analysis with numerical simulations, and proposed a NFW-like triaxial density profile for dark matter halos with quantitative statistics on the distribution of the axial ratios and the concentration parameter. Their studies allow one to investigate the systematic differences caused by the non-sphericity of mass distributions. Significant effects have been found in the statistics of arcs, and the probability of large separation gravitational lenses (e.g., Oguri, Lee & Suto 2003; Meneghetti, Bartelmann & Moscardini 2003; Dalal et al. 2004; Oguri & Keeton 2004).

For clusters of galaxies, the distribution of intra-cluster gas (ICM) is closely associated with the underlying dark matter distribution, and therefore observations, such as X-ray (e.g., Rosati et al. 2002) and Sunyaev-Zeldovich (SZ) effect (e.g., Carlstrom et al. 2002) can provide us information on the dark matter profiles (e.g., Allen et al. 2002; Grego et al. 2004; Grego et al. 2001). Lee & Suto (2003) studied the equilibrium gas distribution in triaxial dark matter halos under the approximation of small ellipticities. They (Lee & Suto 2004) further analyzed the X-ray and SZ effect distributions associated with the triaxial mass distribution of clusters of galaxies. Since they aimed at finding the dark matter distribution for individual clusters, they parametrized the observables (X-ray and SZ) with the parameters being functions of those characterizing the mass profile of dark matter halos. While this type of reconstruction is certainly useful, individuality of clusters affects the results considerably.

On the other hand, for a large number of clusters, one can study collectively the profile of the observables, and further investigate the underlying dark matter distribution statistically. Mohr et al. (1995) analyzed 65 X-ray clusters, and presented statistical results on several quantities representing the morphology of clusters' X-ray emissions. With their limited sample, they found that the distribution of the axial ratio of X-ray emissions has a main peak at $\eta \sim 0.9$ with a minor peak at $\eta \sim 0.6$. The average axial ratio is $\langle \eta \rangle \sim 0.8$. To investigate the three-dimensional ICM distribution, Cooray (2000) assumed a spheroidal ICM profile (prolate or oblate), and obtained statistics of 3-D axial ratio given the 2-D results of Mohr et al. (1995). Similar studies on elliptical galaxies have been carried out for many years (e.g., Binney 1985; Binney & de Vaucouleurs 1981).

The triaxial mass distribution of dark matter obtained from numerical simulations (Jing and Suto 2002) provides us a starting point to study the ICM distribution without artificial assumptions. In this paper, we analyze the corresponding surface profiles of X-ray and SZ effects. Instead of focusing on individual clusters, we investigate the profiles of observables statistically. Specifically the axial-ratio distributions of X-ray and SZ effects profiles resulting from the triaxial dark matter distributions are derived. Our study presents another view to test the theory of the formation of dark matter halos.

The rest of the paper is organized as follows. Under the equilibrium assumption, in §2, we derive the two-dimensional profiles of SZ and X-ray observables from triaxial dark matter distributions. In §3, we obtain the two-dimensional eccentricities of the SZ and X-ray profiles under the linear approximation for the deviation of sphericity. Section 4 presents the statistical analysis on the distribution of two-dimensional eccentricities, which can be compared with observational results. Summary and discussion are given in §5. Appendix A contains derivations of the eccentricities for the isothermal SZ effects. Results for other cases are also presented. Appendix B discusses possible values of the parameter C/K associated with X-rays and SZ effects.

Throughout the paper, we consider the concordance cosmological model with $\Omega_m = 0.3$, $\Omega_\Lambda = 0.7$, $H_0 = 72 \text{ km/s/Mpc}$ and $\sigma_8 = 0.9$, where Ω_m and Ω_Λ are the present dimensionless matter density and the dark energy density of the universe, respectively, H_0 is the present Hubble constant, and σ_8 is rms of the extrapolated linear mass density fluctuation smoothed over $8h^{-1} \text{ Mpc}$ with h the Hubble constant in units of 100 km/s/Mpc .

2. Two-dimensional SZ and X-ray profiles

2.1. Gas density distribution

The three-dimensional triaxial density distribution of dark matter halos is given by Jing & Suto (2002), which has the following form

$$\frac{\rho(R)}{\rho_{crit}} = \frac{\delta_c}{(R/R_0)^\alpha (1 + R/R_0)^{3-\alpha}} \quad (1)$$

where $R = a(x^2/a^2 + y^2/b^2 + z^2/c^2)^{1/2}$ ($c \leq b \leq a$) is the length of the major axis, R_0 is a scale radius, δ_c is a characteristic density and ρ_{crit} is the critical density of the universe. For the value of α , it is found that both $\alpha = 1$ and $\alpha = 1.5$ can fit well to the profiles of simulated dark matter halos. Detailed comparison showed that $\alpha = 1$ is slightly better for cluster-scale halos while for galactic halos, $\alpha = 1.5$ gives better results. In this paper, we focus on clusters of galaxies, and adopt $\alpha = 1.0$.

Under the equilibrium assumption, we can derive the gas distribution in a triaxial dark matter halo. The related equations are the Poisson equation and the equilibrium equation. Specifically,

$$\nabla^2 \Phi = 4\pi G \rho, \quad (2)$$

$$\frac{1}{\rho_g} \nabla P_g = -\nabla \Phi, \quad (3)$$

where Φ is the gravitational potential, ρ is the total matter density, ρ_g is the gas density, and P_g is the gas pressure.

We consider both isothermal and polytropic ICM states. For the isothermal case, we have

$$P_g = \frac{k_B T_g}{\mu m_p} \rho_g \equiv K \rho_g, \quad (4)$$

where k_B , T_g , μ , and m_p represent the Boltzmann constant, the gas temperature, the mean molecular weight, and the proton mass, respectively. Then the gas density is related to the gravitational potential through the following equation

$$\frac{\rho_g}{\rho_{g0}} = \exp\left[-\frac{1}{K}(\Phi - \Phi_0)\right], \quad (5)$$

where the subscript 0 denotes the corresponding value at the central position.

For polytropic gas, the equation of state is

$$P_g = P_{g0} [\rho_g / \rho_{g0}]^\gamma, \quad (6)$$

where γ is the polytropic index. The equilibrium gas density can be derived as

$$\rho_g = \rho_{g0} \left\{ 1 - \frac{1}{K_0} \frac{\gamma - 1}{\gamma} [\Phi - \Phi_0] \right\}^{\frac{1}{\gamma-1}}, \quad (7)$$

where $K_0 = k_B T_{g0} / \mu m_p$ with T_{g0} the central temperature of ICM. It is seen that the gas density profile is closely associated with that of the gravitational potential, and the isopotential contours are also isodensity contours of ICM.

As ICM contributes about 10% of total cluster mass, it is neglected in calculating the gravitational potential. From the triaxial density profile of dark matter halos (eq.[1]), one can solve the Poisson equation to obtain the gravitational potential numerically (e.g., Binney & Tremaine 1987).

Under the approximation of small eccentricities for dark matter halos, Lee and Suto (2003) derived an analytical solution for the gravitational potential, which is given as

$$\Phi(\vec{u}) \approx C \left[F_1(u) + \frac{e_b^2 + e_c^2}{2} F_2(u) + \frac{e_b^2 \sin^2 \theta_0 \sin^2 \varphi_0 + e_c^2 \cos^2 \theta_0}{2} F_3(u) \right], \quad (8)$$

where $\vec{u} \equiv \vec{r}/R_0$, $\vec{r} = (x, y, z) = r(\sin \theta_0 \cos \varphi_0, \sin \theta_0 \sin \varphi_0, \cos \theta_0)$, $C = 4\pi G \delta_c \rho_{crit} R_0^2$, $e_b = (1 - b^2/a^2)^{1/2}$ and $e_c = (1 - c^2/a^2)^{1/2}$. Here e_b and e_c are the two eccentricities of the ellipsoidal dark matter halos. The three functions $F_1(u)$, $F_2(u)$ and $F_3(u)$ are given in Lee and Suto (2003). In the following, our analytical analyses on the two-dimensional SZ and X-ray profiles are obtained primarily from the potential given by equation (8). On the other hand, we also solve for the gravitational potential numerically from Poisson equation, and derive the exact SZ and X-ray profiles. These exact solutions are compared with those analytical ones to test the validity of the approximation underlying equation (8).

For triaxial clusters, their appearances depend on the viewing direction. With (x, y, z) the principal coordinate system, we introduce (x', y', z') with z' the line of sight direction and x' lying in the $x-y$ plane (e.g., Binney 1985; Oguri, Lee & Suto 2003). The two systems are related by

$$\begin{bmatrix} x \\ y \\ z \end{bmatrix} = T \begin{bmatrix} x' \\ y' \\ z' \end{bmatrix}, \quad (9)$$

where

$$T \equiv \begin{bmatrix} -\sin \phi & -\cos \phi \cos \theta & \cos \phi \sin \theta \\ \cos \phi & -\sin \phi \cos \theta & \sin \phi \sin \theta \\ 0 & \sin \theta & \cos \theta \end{bmatrix}. \quad (10)$$

Here θ and ϕ are the polar coordinates of the line of sight direction in the (x, y, z) coordinate system. Then we have

$$\Phi(\vec{u}') \approx C \left[F_1(u') + \frac{e_b^2 + e_c^2}{2} F_2(u') + \frac{e_b^2(x' \cos \phi - y' \sin \phi \cos \theta + z' \sin \phi \sin \theta)^2 + e_c^2(y' \sin \theta + z' \cos \theta)^2}{2r'^2} F_3(u') \right] \quad (11)$$

where $\vec{u}' = \vec{r}'/R_0$.

2.2. SZ and X-ray surface profiles

The typical mass of a cluster of galaxies is $10^{14} - 10^{15} M_\odot$, to which the gas component contributes about 10%. Because of the deep potential well, the typical temperature of ICM is a few keV . Therefore the gas is fully ionized. Hot electrons emit X-ray primarily through thermal bremsstrahlung process. On the other hand, as cosmic microwave background (CMB) photons pass through a cluster, they scatter with free electrons inside. As the result, the CMB spectrum is distorted. This is the thermal SZ effect (Sunyaev & Zel'dovich 1970, 1972). Observing clusters through X-ray and SZ effect has been getting mature, and high resolution imaging of clusters of galaxies is possible. Thus it is becoming observationally feasible to study the ICM distribution and further the underlying dark matter distribution in detail.

Here we derive the respective profiles of SZ effect and X-ray emission from the gas distribution in a triaxial cluster.

The CMB spectrum distortion due to the thermal SZ effect can be described by a frequency-dependent temperature change δT relative to the average CMB temperature. In the nonrelativistic limit, the gas properties affect the SZ effect through the Compton y -parameter, which is proportional to the gas pressure along the line of sight. Specifically, we have

$$\delta T \propto \int n_e T_e dl, \quad (12)$$

where n_e and T_e are the number density and temperature of electrons, respectively. The integration is along the line of sight.

For fully ionized gas primarily consisting of hydrogen and helium, $n_e \propto \rho_g$. Thus

$$\delta T \propto \int \rho_g T_e dl. \quad (13)$$

For isothermal ICM, the SZ effect can then be written as

$$\begin{aligned} \delta T(x', y') &\propto \int \rho_g T_e dl \propto \int \exp\left[-\frac{1}{K}(\Phi - \Phi_0)\right] dl \propto \int \exp\left[-\frac{1}{K}\Phi\right] dl \\ &\propto \int \exp\left\{-\frac{C}{K}\left[F_1(u') + \frac{e_b^2 + e_c^2}{2}F_2(u')\right.\right. \\ &\quad \left.\left. + \frac{e_b^2(x' \cos \phi - y' \sin \phi \cos \theta + z' \sin \phi \sin \theta)^2 + e_c^2(y' \sin \theta + z' \cos \theta)^2}{2r'^2}\right.\right. \\ &\quad \left.\left. F_3(u')\right]\right\} dz'. \end{aligned} \quad (14)$$

For polytropic gas, the SZ effect depends on the potential through the following equation

$$\delta T(x', y') \propto \int \left\{1 - \frac{1}{K_0} \frac{\gamma - 1}{\gamma} [\Phi(x', y', z') - \Phi_0]\right\}^{\frac{\gamma}{\gamma-1}} dz'. \quad (15)$$

For bremsstrahlung X-ray emission, its surface brightness has a different dependence on the density and the temperature of electrons, which is

$$S_x \propto \int n_e^2 \Lambda_{eH} dl, \quad (16)$$

where Λ_{eH} is the X-ray cooling function. For bolometric bremsstrahlung emission, we adopt an approximate expression $\Lambda_{eH} \propto T_e^{1/2}$. In the case of isothermal gas, the above equation is reduced to

$$S_x \propto \int n_e^2 dl, \quad (17)$$

and then we get

$$\begin{aligned} S_X(x', y') &\propto \int \exp\left\{-\frac{2C}{K}\left[F_1(u') + \frac{e_b^2 + e_c^2}{2}F_2(u')\right.\right. \\ &\quad \left.\left. + \frac{e_b^2(x' \cos \phi - y' \sin \phi \cos \theta + z' \sin \phi \sin \theta)^2 + e_c^2(y' \sin \theta + z' \cos \theta)^2}{2r'^2}\right.\right. \\ &\quad \left.\left. F_3(u')\right]\right\} dz'. \end{aligned} \quad (18)$$

For polytropic gas, we have

$$S_X(x', y') \propto \int \left\{1 - \frac{1}{K_0} \frac{\gamma - 1}{\gamma} [\Phi(x', y', z') - \Phi_0]\right\}^{\frac{3+\gamma}{2(\gamma-1)}} dz'. \quad (19)$$

In next section, we demonstrate that both $\delta T(x', y')$ and $S_X(x', y')$ can be well described by a series of concentric ellipses, and we further derive an approximate analytic expression for their axial ratios.

3. Two-dimensional eccentricities of SZ effect and X-ray surface brightness profiles

Lee and Suto (2003) showed that the 3-D gas distribution in a triaxial dark matter halo is approximately ellipsoidal with decreasing eccentricities from the center to the outer part of the cluster. Therefore we expect elliptical-like profiles for both SZ effects and X-ray emissions.

Let ξ be defined as:

$$\xi^2 = \frac{1}{R_0^2} \left(\frac{x''^2}{1 + \Delta} + \frac{y''^2}{1 + \Delta'} \right), \quad (20)$$

where the coordinates (x'', y'') relate to (x', y') by

$$\begin{bmatrix} x' \\ y' \end{bmatrix} = \begin{bmatrix} \cos \Psi & -\sin \Psi \\ \sin \Psi & \cos \Psi \end{bmatrix} \begin{bmatrix} x'' \\ y'' \end{bmatrix}. \quad (21)$$

The form ξ given in equation (20) represents that the length of both the major and minor axes is different from the circular radius $\tilde{r}'' = \sqrt{x''^2 + y''^2}$. From the view point of small aspherical perturbations, a circle of \tilde{r}'' is perturbed to an ellipse labeled by ξ . On the other hand, for an elliptical form $\tilde{\xi}^2 = (1/R_0^2)[x''^2 + y''^2/(1 + \Delta'')]$, only one of the two axes is perturbed away from the circle. In other words, with same ξ and $\tilde{\xi}$, the corresponding original circles \tilde{r}'' are different. From Appendix A (A13), we see that ξ in equation (20) is in general consistent with the perturbative results. Only in the case of $e_c = 0$ or $\theta = 0$, $\tilde{\xi}$ gives a valid description.

To approximate the distributions of SZ effects or X-ray emissions with a series of ellipses, we assume that the 2-D observables are functions of ξ only. Thus Ψ represents the orientation of an elliptical contour in (x', y') coordinate system. With tedious but straightforward derivations, which are shown in Appendix A for the isothermal SZ effects, we obtain, to the leading order of e_b^2 and e_c^2 , the following general expressions for all the cases considered

$$\tan 2\Psi = \frac{C_{13}}{C_{11} - C_{12}}, \quad (22)$$

$$\Delta = - \left[-C_{13} \sqrt{1 + \left(\frac{C_{11} - C_{12}}{C_{13}} \right)^2} + (C_{11} + C_{12}) \right] M(\tilde{u}'), \quad (23)$$

$$\Delta' = - \left[C_{13} \sqrt{1 + \left(\frac{C_{11} - C_{12}}{C_{13}} \right)^2} + (C_{11} + C_{12}) \right] M(\tilde{u}'), \quad (24)$$

and

$$E^2 = 1 - \frac{1 + \Delta}{1 + \Delta'} = \frac{\Delta' - \Delta}{1 + \Delta'} \approx \Delta' - \Delta = 2C_{13} \sqrt{1 + \left(\frac{C_{11} - C_{12}}{C_{13}}\right)^2} [-M(\tilde{u}')], \quad (25)$$

where E is the eccentricity, and

$$C_{11} = -e_b^2 \cos^2 \phi, \quad (26)$$

$$C_{12} = -(e_b^2 \sin^2 \phi \cos^2 \theta + e_c^2 \sin^2 \theta), \quad (27)$$

$$C_{13} = e_b^2 \sin 2\phi \cos \theta, \quad (28)$$

and M is a function of $\tilde{u}' = (\sqrt{x'^2 + y'^2})/R_0$ only. The specific functional forms of M for different cases can be found in Appendix A.

From the above perturbative results, we see explicitly that for a relaxed cluster of galaxies, Ψ is independent of \tilde{u}' , i.e., the elliptical contours of an observable are in alignment with each other. For the eccentricity, its \tilde{u}' and line-of-sight (θ, ϕ) dependences are separable. The \tilde{u}' -dependent factor M reflects the differences between the distribution of dark matter and that of the ICM, and is specific for different quantities, SZ effects or X-ray emissions.

It is clear to see that the 2-D eccentricity E is on the order of e_b or e_c of the underlying dark matter halo. For a cluster, the value of E is very similar for the four considered cases. Figure 1 shows the eccentricity of the isothermal SZ profiles at different radius. The parameters of the cluster are chosen to be $M = 10^{14} h^{-1} M_\odot$, $e_b = 0.6$, and $e_c = 0.8$. The concentration parameter is taken to be the corresponding average value (Jing & Suto 2002). The line-of-sight direction lies in $\theta = 0$ and $\phi = 0$. For this set of parameters, the perturbative result is $E = e_b \sqrt{-2M(\tilde{u}')}$, which is shown as the solid line. The dotted line is the exact result from direct numerical calculations without approximations. It is seen that the perturbative eccentricity is systematically higher than that of the numerical one, but not by a large fraction. The differences between the two do not exceed $\sim 17\%$ for \tilde{u}' up to 10. In terms of the axial ratio η , the corresponding differences are less than $\sim 5\%$. For smaller e_b and e_c , the perturbative and numerical results agree better. Thus our approximate expressions describe the profiles of SZ effect and X-ray emission reasonably well. There is a mild change of E with radius. At the central region $E \sim 0.5$, which corresponds to the axial ratio $\eta \sim 0.87$. In the region around the virial radius, $E \sim 0.38$ and $\eta \sim 0.93$.

Stark (1977) studied triaxial models of the bulge of M31. Assuming an ellipsoidal volume brightness distribution with constant axial ratios, $x^2 + (uy)^2 + (tz)^2 = a_v^2$, he derived the surface isophotes, and obtained a series of similar ellipses with their axial ratio depending on u, t and the line-of-sight direction. Specifically for the line-of-sight direction shown in Figure 1, the axial ratio of isophotes is $\beta = 1/u$, or the eccentricity $\sqrt{1 - (1/u)^2}$. In the problem we analyze here, it is the dark matter halo that has an ellipsoidal configuration with constant

e_b and e_c . For the equilibrium ICM, it distributes more spherically than that of the dark matter with scale-dependent asphericity. Then our result $E = e_b \sqrt{[-2M(\tilde{u}')]}$ can be clearly understood: e_b is the eccentricity of the dark matter halo in the line-of-sight direction, and the factor $\sqrt{[-2M(\tilde{u}')]}$ shows the differences between the distributions of dark matter and ICM. The value of E is smaller than $e_b = 0.6$.

4. Statistical analysis for the eccentricity distribution

In this section, we investigate the expected statistical distributions of E (or equivalently the axial ratio η) of 2-D observables if dark matter halos of clusters of galaxies do have triaxial mass distributions as revealed by numerical simulations. Our theoretical results can be potentially confronted with observational results, and the agreement/disagreement between the two can be used as evidences supporting/challenging the cold dark matter structure formation scenario.

As shown in equation (25), the eccentricity is a function of $(e_b, e_c, c_e, \theta, \phi)$. Thus its statistical distribution can be calculated through the distributions of the five quantities. For a sample of clusters of mass M at redshift z , the differential distribution function $p(E^2)$ has the form

$$p(E^2)dE^2 = \left[\frac{2}{\pi} \int p(c/a)d(c/a) \int p(c/b | c/a)d(c/b) \int p(c_e)dc_e \int \left(\frac{\partial E^2}{\partial \phi} \right)_{\theta, c_e, c/b, c/a}^{-1} \sin \theta d\theta \right] dE^2, \quad (29)$$

where the inner most integral reflects the projection effect, i.e., the change of the appearance of a fixed cluster due to different viewing. The other three integrals are for the distributions of the concentration parameter c_e , and the two axial ratios c/a and c/b given by Jing and Suto (2002).

Before going to the full distribution of equation (29), we first study the distribution of E^2 due solely to the projection effect, which can be calculated through

$$p(E^2 | c_e, c/b, c/a) = \frac{2}{\pi} \int_{\theta_1}^{\theta_2} \left(\frac{\partial E^2}{\partial \phi} \right)_{\theta, c_e, c/b, c/a}^{-1} \sin \theta d\theta \quad (30)$$

where (θ_1, θ_2) is the range of θ in which a physically meaningful value of ϕ can be found for a fixed value of E^2 (Binney & de Vaucouleurs 1981).

In Figure 2, we show $p(E^2 | c_e, c/b, c/a)$ of the isothermal SZ effect for a cluster of mass $M = 10^{14} h^{-1} M_\odot$ at $z = 0$. Three sets of (e_b, e_c) are considered. In all the cases, there are two peaks in the distribution, which correspond to the two largest apparent axial ratios when viewed along the cluster's principal axes. Specifically in our definition of the coordinate

systems, the two line of sights are $\theta = 0$ and $(\theta = \pi/2, \phi = 0)$, respectively. Our results are consistent with the study of Binney and de Vaucouleurs (1981) for elliptical galaxies. Note that e_b and e_c are the eccentricities of the dark matter halo and the 3-D gas profile is rounder than that of the dark matter distribution.

Now let us consider the full probability function. The relevant distributions are taken from Jing and Suto (2002). Specifically we adopt (Oguri, Lee & Suto 2003)

$$p(c/a) = \frac{1}{\sqrt{2\pi} \times 0.113} \exp \left\{ - \frac{[(c/a)(M_{vir}/M_\star)^{0.07\Omega(z)^{0.7}} - 0.54]^2}{2(0.113)^2} \right\} \left(\frac{M_{vir}}{M_\star} \right)^{0.07\Omega(z)^{0.7}}, \quad (31)$$

where M_\star is the characteristic nonlinear mass scale satisfying $\sigma(M_\star) = 1.68$ with $\sigma(M_\star)$ the rms of linear density fluctuations smoothed over mass scale M_\star , and

$$p(c/b | c/a) = \frac{3}{2(1 - r_{min})} \left[1 - \left(\frac{2c/b - 1 - r_{min}}{1 - r_{min}} \right)^2 \right], \quad (32)$$

for $c/b \geq r_{min}$, where $r_{min} = c/a$ for $c/a \geq 0.5$ and $r_{min} = 0.5$ for $c/a < 0.5$. For $c/b \leq r_{min}$, $p(c/b | c/a) = 0$. For the concentration parameter c_e , we have

$$p(c_e) = \frac{1}{\sqrt{2\pi} \times 0.3} \exp \left[- \frac{(\ln c_e - \ln \bar{c}_e)^2}{2(0.3)^2} \right] \frac{1}{c_e}, \quad (33)$$

where the fitting formula of \bar{c}_e in the triaxial model is given by:

$$\bar{c}_e = 1.35 \exp \left\{ - \left[\frac{0.3}{(c/a)(M_{vir}/M_\star)^{0.07\Omega(z)^{0.7}}} \right]^2 \right\} A_e \sqrt{\frac{\Delta_{vir}(z_c)}{\Delta_{vir}(z)} \frac{\Omega(z)}{\Omega(z_c)}} \left(\frac{1 + z_c}{1 + z} \right)^{3/2} \quad (34)$$

where z_c is the collapse redshift of the cluster of mass M_{vir} and $\Delta_{vir}(z)$ is the average density of a virialized halo with respect to the critical density, i.e., $\Delta_{vir}(z) \equiv (3M_{vir})/(4\pi r_{vir}^3 \rho_{crit})$. For the numerical factor A_e , we take $A_e = 1.1$.

In Figure 3, the probability functions are shown for the four cases we discussed. To be more comparable with the results of Mohr et al. (1995), here and after we change $p(E^2)$ to $f(\eta)$, the probability function of the axial ratio η . The cluster mass is taken to be $M_{vir} = 10^{14} h^{-1} M_\odot$ and is placed at redshift $z = 0$. For all the four cases, $f(\eta)$ are very similar with a peak at $\eta \sim 0.9$ and a tail extended to $\eta \sim 0.6$. In the following study, we concentrate on $f(\eta)$ of the isothermal SZ effect.

Figure 4 demonstrates the dependence of $f(\eta)$ on the cluster mass (left) and on the redshift (right). For larger clusters, the SZ profiles become more elongated, with the peak of $f(\eta)$ moving from $\eta \sim 0.9$ for $M_{vir} = 10^{14} h^{-1} M_\odot$ to $\eta \sim 0.85$ for $M_{vir} = 10^{15} h^{-1} M_\odot$. On the other hand, $f(\eta)$ does not show significant redshift evolution.

The above statistics focused on cluster samples with fixed masses and at fixed redshifts. Observationally, a cluster sample is often flux limited so that the sample contains clusters of various masses at different redshifts. Under the equilibrium assumption, a flux limit (SZ effect or X-ray) can be converted to a mass limit which is redshift dependent. Thus in the following we consider mass limited cluster samples. For simplicity, however, we choose a redshift-independent mass limit M_{lim} for each sample. To certain extents, SZ-selected clusters are more or less fixed-mass-selected clusters (Holder et al. 2000). For a mass limited sample, the probability density $f(\eta)$ can be calculated through

$$f(\eta) = \frac{\int dV(z) \int_{M_{lim}} f(\eta)|_{M,z} (dn/dM) dM}{\int (dn/dM) dM dV}, \quad (35)$$

where $f(\eta)|_{M,z}$ is the probability density of η for clusters of fixed mass M at redshift z analyzed above, $(dn/dM)dM$ is the number density of clusters of mass $(M, M + dM)$, and dV is the volume element.

For the number density of clusters, we adopt the one from Jenkins et al. (2001)

$$\begin{aligned} \frac{dn}{dM}(z, M) &= 0.315 \frac{\rho_0}{M \sigma_M} \left| \frac{d\sigma_M}{dM} \right| \\ &\times \exp[-|0.61 - \ln(D_z \sigma_M)|^{3.8}], \end{aligned} \quad (36)$$

where ρ_0 is the present matter density of the universe, D_z is the linear growth factor, and σ_M is the rms of the linearly extrapolated-to-present matter density fluctuation over the mass scale M , which is given by Viana & Liddle (1999)

$$\sigma_M = \sigma_8 \left[\frac{R(M)}{8h^{-1}Mpc} \right]^{-\gamma[R(M)]} \quad (37)$$

where $R(M)$ is the comoving radius corresponding to M , and γ has the following form

$$\gamma(R) = (0.3\Gamma + 0.2) \left[2.92 + \log_{10} \left(\frac{R}{8h^{-1}Mpc} \right) \right] \quad (38)$$

with Γ the shape parameter.

In the left panel of Figure 5, the mass limited $f(\eta)$ of the isothermal SZ effect is shown for $M_{lim} = 10^{13}h^{-1}M_\odot$ and $M_{lim} = 10^{14}h^{-1}M_\odot$, respectively. The axial ratio is calculated at the virial radius r_{vir} . It is seen that for the cluster sample with a larger M_{lim} , the distribution $f(\eta)$ has a peak at a smaller η and extends more toward elongated configurations. The average axial ratio $\langle \eta \rangle \approx 0.87$ and 0.84 for $M_{lim} = 10^{13}h^{-1}M_\odot$ and $M_{lim} = 10^{14}h^{-1}M_\odot$, respectively. Although only the results for the SZ effect are shown here, we expect similar $f(\eta)$ for X-ray emission profiles.

The measurements of Mohr et al.(1995) on the emission-weighted axial ratio for 57 X-ray clusters gave $\langle\eta\rangle \approx 0.8$. The distribution has a major peak at $\eta \sim 0.9$ and a minor one at $\eta \sim 0.6$. They compared the results with those of numerical simulations of different cosmologies. Due to the strong dynamical evolution of clusters, the profiles of X-ray emissions show significant non-sphericity for $\Omega_m = 1$ model with $\langle\eta\rangle \approx 0.7$. For low density models, the late time evolution of clusters is weak, and the clusters are nearly spherical with $\langle\eta\rangle \approx 0.95$ for $(\Omega_m = 0.2, \Omega_\Lambda = 0)$ and $\langle\eta\rangle \approx 0.91$ for $(\Omega_m = 0.2, \Omega_\Lambda = 0.8)$. The observational $f(\eta)$ lies in between the models of $\Omega_m = 1$ and $\Omega_m = 0.2$. Our analysis presented here is for the cosmological model $(\Omega_m = 0.3, \Omega_\Lambda = 0.7)$. For $M_{lim} = 10^{14}h^{-1}M_\odot$, we have $\langle\eta\rangle \approx 0.84$, which is very close to the observational value of $\langle\eta\rangle \approx 0.8$. On the other hand, there are several differences between our idealized cluster sample and the observational sample of Mohr et al. (1995), so that the comparison of the two is tentative. Firstly, their sample is more or less a flux limited sample with some complications (Mohr et al. 1995; Edge et al. 1990), while our analysis is performed on a mass limited sample. Secondly, their statistics is on the emission-weighted axial ratio that emphasizes more on the core structure. Our results in the left panel of Figure 5 are for $\tilde{r}' = r_{vir}$. We have known that the ellipticities of the SZ effect and X-ray profiles are higher for the central region of a cluster than that of the outer part (see Figure 1). Therefore we expect smaller $\langle\eta\rangle$ for the emission-weighted axial ratio in our model, which would be closer to the observational results. For the purpose of demonstration, in the right panel of Figure 5, we show the results for $\tilde{r}' = r_{vir}$ and $\tilde{r}' = 0.7r_{vir}$, respectively, for $M_{lim} = 10^{13}h^{-1}M_\odot$. The respective average axial ratios are $\langle\eta\rangle \approx 0.87$ and 0.86 .

The minor peak revealed by Mohr et al. (1995) does not show up in our theoretical analysis. Whether this is a serious problem for the model is not clear since the number of observed clusters (57) is still not large enough for a solid statistical conclusion on the appearance of the low peak. This minor peak may just represent the tail of the distribution.

5. Summary and Discussion

X-ray emission and SZ effect from a cluster of galaxies are directly related to the hot ICM, which is gravitationally bound to the deep potential well of dark matter halos of clusters. Therefore, different from optically selected clusters whose identifications are affected considerably by the projection effects, X-ray or SZ selected clusters are relatively clean. Further more, the continuous distribution makes the ICM a better tracer of the overall underlying dark matter than galaxies. Thus X-ray and SZ observations have been used extensively to study the distribution of dark matter (e.g., Buote and Lewis 2004).

Based on the triaxial dark matter halo model from numerical simulations, we derived

the profiles of SZ effects and X-ray emissions for clusters of galaxies. It is found that they can be well described by a set of concentric ellipses with the eccentricity E decreasing toward the outer part of a cluster. Under the approximation that the triaxiality of dark matter halos is weak, we obtained an analytical expression for eccentricities of these observables, which is a function of e_b , e_c , c_e , θ and ϕ . Here the first three quantities represent the intrinsic shape of dark matter halos, and the last two label the line-of-sight direction. For the four cases we discussed (SZ/X-ray, isothermal/polytropic), the elongation of the profiles is similar. For a halo of $M = 10^{14}h^{-1}M_\odot$ and $e_b = 0.6$ and $e_c = 0.8$, $E \sim 0.4$ for $\theta = 0$ and $\phi = 0$.

Our analytical results of (22) to (25) can be potentially used to constrain the dark matter distribution of a cluster from the corresponding observations of Ψ and E . Unfortunately, the line-of-sight direction (θ, ϕ) cannot be known beforehand, which strongly limits the reconstruction of dark matter distribution from X-ray and SZ observations for individual clusters. However, given Ψ and E , certain constraints on (θ, ϕ) and therefore e_b and e_c can be obtained. For example, as shown in Figure 1, with $\Psi = 0$, the observed E at the central region of a cluster puts a lower limit on e_b .

On the other hand, analyses on the distribution of E for a sample of clusters can probe the asphericity of dark matter distribution statistically. With the knowledge of the distributions of the five parameters, we calculate the statistics of the 2-D eccentricity or equivalently the axial ratio η . We found that for clusters of mass $M = 10^{13}h^{-1}M_\odot$, $\langle\eta\rangle \sim 0.89$, and $\langle\eta\rangle \sim 0.85$ for $M = 10^{15}h^{-1}M_\odot$. The distribution $f(\eta)$ depends very weakly on the redshift. We further studied $f(\eta)$ for mass-limited cluster samples. For $M_{lim} = 10^{13}h^{-1}M_\odot$, $\langle\eta\rangle \sim 0.87$. For $M_{lim} = 10^{14}h^{-1}M_\odot$, $\langle\eta\rangle \sim 0.84$.

Keeping in mind many differences between our idealized cluster samples and the real observational one, we made a tentative comparison with the emission-weighted η distribution of Mohr et al. (1995) for 57 X-ray clusters. Their statistics showed that $\langle\eta\rangle \sim 0.8$. Our analysis for $M_{lim} = 10^{14}h^{-1}M_\odot$ gave $\langle\eta\rangle \sim 0.84$ at $r = r_{vir}$. Since emission-weighted η is influenced more by the central part of a cluster, a smaller $\langle\eta\rangle$ is expected if a similar weighting is done in our theoretical analysis, which would bring a better agreement between the theoretical result and the observational one.

Comparing with results of numerical simulations on different cosmologies, Mohr et al. (1995) concluded that low density models with $\Omega_m = 0.2$ cannot explain the observed morphology of clusters of galaxies. Although our theoretical analysis based on the concordance model with $\Omega_m = 0.3$ and $\Omega_\Lambda = 0.7$ shows a certain degree of consistency with that of observations, some discrepancies as noted by Mohr et al. (1995) are apparent. The model tends to produce more spherical clusters than the observed ones. Gravitationally it is related to the weak dynamical evolution of dark matter halos for low-density models. In our study,

hydrostatic equilibrium is assumed for ICM, and thus the gas distribution is determined fully by the dark matter distribution. In reality, physical processes other than gravity can affect properties of ICM, and change its equilibrium profile considerably.

On the other hand, the observational sample of Mohr et al. (1995) contains 65 clusters (the axial ratio statistics is presented for 57 clusters), and it is still not large enough for a solid conclusion on the morphological statistics. Currently, a large number of high resolution images of clusters are available. Detailed studies on their morphologies are definitely desirable. Because of the much better quality of images, we expect that tighter constraints on theoretical models of structure formation can be obtained through morphological studies on clusters of galaxies.

We sincerely thank the referee for the constructive and detailed comments and suggestions. This research was supported in part by the National Science Foundation of China under grants 10243006 and 10373001, and by the Ministry of Science and Technology of China under grant TG1999075401.

A. Appendix

In this appendix, we present the derivation for the 2-D eccentricity under the approximation of small e_b and e_c .

To the linear order of Δ and Δ' , from equation (20) we have

$$\begin{aligned}\xi &\approx \frac{1}{R_0}(x''^2 - \Delta x''^2 + y''^2 - \Delta' y''^2)^{\frac{1}{2}} \\ &= \frac{\sqrt{x''^2 + y''^2}}{R_0} \left(1 - \frac{\Delta x''^2 + \Delta' y''^2}{x''^2 + y''^2}\right)^{\frac{1}{2}} \\ &\approx \frac{r''}{R_0} \left(1 - \frac{1}{2} \frac{\Delta x''^2 + \Delta' y''^2}{\tilde{r}''^2}\right),\end{aligned}\tag{A1}$$

where $\tilde{r}''^2 = x''^2 + y''^2$. In (x', y') , the above equation becomes

$$\begin{aligned}\xi &= \tilde{u}' \left[1 - \frac{\Delta(x' \cos \Psi + y' \sin \Psi)^2}{2\tilde{r}''^2} - \frac{\Delta'(y' \cos \Psi - x' \sin \Psi)^2}{2\tilde{r}''^2}\right] \\ &= \tilde{u}' \left[1 - \frac{(\Delta \sin^2 \Psi + \Delta' \cos^2 \Psi) \sin^2 \theta' + (\Delta \cos^2 \Psi + \Delta' \sin^2 \Psi) \cos^2 \theta'}{2}\right. \\ &\quad \left. - \frac{(\frac{1}{2}\Delta \sin 2\Psi - \frac{1}{2}\Delta' \sin 2\Psi) \sin 2\theta'}{2}\right],\end{aligned}\tag{A2}$$

where $\tilde{u}' = \tilde{r}'/R_0 = \sqrt{x'^2 + y'^2}/R_0$, and $(x', y') = (\tilde{r}' \cos \theta', \tilde{r}' \sin \theta')$.

Our task is to determine the corresponding Δ , Δ' and Ψ from the profiles derived from the triaxial dark matter distribution. For all the four cases discussed above, the derivations are similar. In the following, we focus on the isothermal SZ profiles.

For $\delta T(x', y') = \delta T(\xi)$, we expand $\delta T(\xi)$ with respect to Δ and Δ' . To the linear order, we have

$$\begin{aligned} \delta T(\xi) &\approx \delta T \left\{ \tilde{u}' \left[1 - \frac{(\Delta \sin^2 \Psi + \Delta' \cos^2 \Psi) \sin^2 \theta' + (\Delta \cos^2 \Psi + \Delta' \sin^2 \Psi) \cos^2 \theta'}{2} \right. \right. \\ &\quad \left. \left. - \frac{(\frac{1}{2}\Delta \sin 2\Psi - \frac{1}{2}\Delta' \sin 2\Psi) \sin 2\theta'}{2} \right] \right\} \\ &\approx \delta T(\tilde{u}') - \frac{\partial \delta T(\tilde{u}')}{\partial \tilde{u}'} \tilde{u}' \left[\frac{(\Delta \sin^2 \Psi + \Delta' \cos^2 \Psi) \sin^2 \theta' + (\Delta \cos^2 \Psi + \Delta' \sin^2 \Psi) \cos^2 \theta'}{2} \right. \\ &\quad \left. + \frac{(\frac{1}{2}\Delta \sin 2\Psi - \frac{1}{2}\Delta' \sin 2\Psi) \sin 2\theta'}{2} \right] \end{aligned} \quad (\text{A3})$$

On the other hand, with $f(u') = (-C/K)[F_1(u') + (1/2)(e_b^2 + e_c^2)F_2(u')]$, equation (14) can be approximately written as:

$$\begin{aligned} \delta T(x', y') &\propto \int \exp[f(u')] \left[1 - \frac{C}{K} F_3(u') \right. \\ &\quad \left. \frac{e_b^2 (x' \cos \phi - y' \sin \phi \cos \theta + z' \sin \phi \sin \theta)^2 + e_c^2 (y' \sin \theta + z' \cos \theta)^2}{2r'^2} \right] dz' \\ &= \int \exp[f(u')] dz' - \frac{C}{K} \int \exp[f(u')] F_3(u') \\ &\quad \left[\frac{e_b^2 (x' \cos \phi - y' \sin \phi \cos \theta + z' \sin \phi \sin \theta)^2 + e_c^2 (y' \sin \theta + z' \cos \theta)^2}{2r'^2} \right] dz' \\ &= \int \exp[f(u')] dz' - \frac{C}{KR_0^2} [(e_b^2 \cos^2 \phi)x'^2 + (e_b^2 \sin^2 \phi \cos^2 \theta + e_c^2 \sin^2 \theta)y'^2 \\ &\quad - (2e_b^2 \sin \phi \cos \phi \cos \theta)x'y'] \int \exp[f(u')] \frac{F_3(u')}{2u'^2} dz' \\ &\quad - \frac{C}{KR_0^2} (e_b^2 \sin^2 \phi \sin^2 \theta + e_c^2 \cos^2 \theta) \int \exp[f(u')] F_3(u') \frac{z'^2}{2u'^2} dz' \end{aligned} \quad (\text{A4})$$

The above approximation assumed that the non-circular part of δT is small due to the small values of e_b and e_c . The validity of this assumption depends on the value of C/K , which is related to the concentration parameter of the dark halo. In Figure 6, we showed the comparisons between the approximate results [equation (A4) for isothermal δT] and those

from the direct integrations of equations given in the previous section [equation (14) for the isothermal δT] for the isothermal SZ (left) and X-rays (right) for several different values of C/K . It is seen that the two agree very well for reasonable C/K values, which are discussed in Appendix B.

Let us define

$$\begin{aligned}\hat{F}_{11}(\tilde{u}') &= \int \exp[f(u')] dz' \\ &= \int \exp \left\{ -\frac{C}{K} \left[F_1(u') + \frac{e_b^2 + e_c^2}{2} F_2(u') \right] \right\} dz',\end{aligned}\quad (\text{A5})$$

$$\begin{aligned}\hat{F}_{12}(\tilde{u}') &= \int \exp[f(u')] F_3(u') \frac{z'^2}{2u'^2} dz' \\ &= \int \exp \left\{ -\frac{C}{K} \left[F_1(u') + \frac{e_b^2 + e_c^2}{2} F_2(u') \right] \right\} F_3(u') \frac{z'^2}{2u'^2} dz',\end{aligned}\quad (\text{A6})$$

$$\begin{aligned}\hat{F}_{13}(\tilde{u}') &= \frac{C}{K} \int \exp[f(u')] \frac{F_3(u')}{2u'^2} dz' \\ &= \frac{C}{K} \int \exp \left\{ -\frac{C}{K} \left[F_1(u') + \frac{e_b^2 + e_c^2}{2} F_2(u') \right] \right\} \frac{F_3(u')}{2u'^2} dz',\end{aligned}\quad (\text{A7})$$

and

$$C_{11} = -e_b^2 \cos^2 \phi, \quad (\text{A8})$$

$$C_{12} = -(e_b^2 \sin^2 \phi \cos^2 \theta + e_c^2 \sin^2 \theta), \quad (\text{A9})$$

$$C_{13} = e_b^2 \sin 2\phi \cos \theta. \quad (\text{A10})$$

Then we have

$$\begin{aligned}\delta T(x', y') &\propto \hat{F}_{11}(\tilde{u}') - \frac{C}{KR_0^2} (e_b^2 \sin^2 \theta \cos^2 \phi + e_c^2 \cos^2 \theta) \hat{F}_{12}(\tilde{u}') \\ &\quad + \frac{1}{R_0^2} (C_{11} x'^2 + C_{12} y'^2 + C_{13} x' y') \hat{F}_{13}(\tilde{u}') \\ &= \hat{F}_{11}(\tilde{u}') - \frac{C}{KR_0^2} (e_b^2 \sin^2 \theta \cos^2 \phi + e_c^2 \cos^2 \theta) \hat{F}_{12}(\tilde{u}') \\ &\quad + (C_{11} \cos^2 \theta' + C_{12} \sin^2 \theta' + C_{13} \cos \theta' \sin \theta') \hat{F}_{13}(\tilde{u}') \tilde{u}'^2\end{aligned}\quad (\text{A11})$$

Comparing with equation (A3), we obtain

$$\delta T(\xi) \propto \hat{F}_{11}(\xi) - \frac{C}{KR_0^2} (e_b^2 \sin^2 \theta \cos^2 \phi + e_c^2 \cos^2 \theta) \hat{F}_{12}(\xi). \quad (\text{A12})$$

Then to the linear order of e_b^2 and e_c^2 , Δ , Δ' and Ψ are determined by the following relations

$$\begin{cases} \frac{\partial \hat{F}_{11}(\tilde{u}')}{\partial \tilde{u}'} \left(-\frac{\Delta \cos^2 \Psi + \Delta' \sin^2 \Psi}{2} \right) = C_{11} \hat{F}_{13} \tilde{u}' \\ \frac{\partial \hat{F}_{11}(\tilde{u}')}{\partial \tilde{u}'} \left(-\frac{\Delta \sin^2 \Psi + \Delta' \cos^2 \Psi}{2} \right) = C_{12} \hat{F}_{13} \tilde{u}' \\ \frac{\partial \hat{F}_{11}(\tilde{u}')}{\partial \tilde{u}'} \left(-\frac{\Delta \sin 2\Psi - \Delta' \sin 2\Psi}{2} \right) = C_{13} \hat{F}_{13} \tilde{u}'. \end{cases} \quad (\text{A13})$$

Explicitly, we have

$$\tan 2\Psi = \frac{C_{13}}{C_{11} - C_{12}}, \quad (\text{A14})$$

$$\Delta = -[-C_{13} \sqrt{1 + \left(\frac{C_{11} - C_{12}}{C_{13}}\right)^2} + (C_{11} + C_{12})] M_1(\tilde{u}'), \quad (\text{A15})$$

$$\Delta' = -[C_{13} \sqrt{1 + \left(\frac{C_{11} - C_{12}}{C_{13}}\right)^2} + (C_{11} + C_{12})] M_1(\tilde{u}'), \quad (\text{A16})$$

and

$$E^2 = 1 - \frac{1 + \Delta}{1 + \Delta'} = \frac{\Delta' - \Delta}{1 + \Delta'} \approx \Delta' - \Delta = 2C_{13} \sqrt{1 + \left(\frac{C_{11} - C_{12}}{C_{13}}\right)^2} [-M_1(\tilde{u}')], \quad (\text{A17})$$

where $M_1(\tilde{u}') = \tilde{u}' \hat{F}_{13}(\tilde{u}') / \partial_{\tilde{u}'} \hat{F}_{11}(\tilde{u}')$

For the other three cases, the only difference is showed up in the M factor, $M_i(\tilde{u}') = \tilde{u}' \hat{F}_{i3}(\tilde{u}') / \partial_{\tilde{u}'} \hat{F}_{i1}(\tilde{u}')$, where i indicates different observables.

For isothermal X-ray emission,

$$\hat{F}_{21}(\tilde{u}') = \int \exp \left\{ -\frac{2C}{K} \left[F_1(u') + \frac{e_b^2 + e_c^2}{2} F_2(u') \right] \right\} dz', \quad (\text{A18})$$

$$\hat{F}_{23}(\tilde{u}') = \frac{2C}{K} \int \exp \left\{ -\frac{2C}{K} \left[F_1(u') + \frac{e_b^2 + e_c^2}{2} F_2(u') \right] \right\} \frac{F_3(u')}{2u'^2} dz'. \quad (\text{A19})$$

For polytropic SZ effect,

$$\hat{F}_{31}(\tilde{u}') = \int \left\{ 1 - \frac{C}{K_0} \frac{\gamma - 1}{\gamma} \left[F_1(u') + \frac{e_b^2 + e_c^2}{2} F_2(u') - \frac{\Phi_0}{C} \right] \right\}^{\gamma/(\gamma-1)} dz', \quad (\text{A20})$$

$$\hat{F}_{33}(\tilde{u}') = \frac{C}{K_0} \int \left\{ 1 - \frac{C}{K_0} \frac{\gamma - 1}{\gamma} \left[F_1(u') + \frac{e_b^2 + e_c^2}{2} F_2(u') - \frac{\Phi_0}{C} \right] \right\}^{1/(\gamma-1)} \frac{F_3(u')}{2u'^2} dz' \quad (\text{A21})$$

For polytropic X-ray emission,

$$\hat{F}_{41}(\tilde{u}') = \int \left\{ 1 - \frac{C}{K_0} \frac{\gamma - 1}{\gamma} \left[F_1(u') + \frac{e_b^2 + e_c^2}{2} F_2(u') - \frac{\Phi_0}{C} \right] \right\}^{(3+\gamma)/[2(\gamma-1)]} dz' \quad (\text{A22})$$

$$\hat{F}_{43}(\tilde{u}') = \frac{C}{K_0} \frac{3+\gamma}{2\gamma} \int \left\{ 1 - \frac{C}{K_0} \frac{\gamma - 1}{\gamma} \left[F_1(u') + \frac{e_b^2 + e_c^2}{2} F_2(u') - \frac{\Phi_0}{C} \right] \right\}^{(5-\gamma)/[2(\gamma-1)]} \frac{F_3(u')}{2u'^2} dz' \quad (\text{A23})$$

B. Appendix

The parameter C/K (C/K_0 for polytropic case) is related to the characteristic density of dark matter halos and the temperature information of ICM. Specifically, we have

$$\frac{C}{K} = \frac{4\pi G \delta_c \rho_{crit} R_0^2}{(k_B T_g / \mu m_p)}. \quad (\text{B1})$$

The value of C/K depends on boundary conditions.

Since we only consider nonspherical mass distribution up to e_b^2 and e_c^2 , C/K can be estimated under the spherical assumption. For isothermal ICM, the equilibrium equation tells us

$$\frac{dp_g}{dr} = -\rho_g \frac{d\Phi}{dr}, \quad (\text{B2})$$

and from it, we obtain

$$\frac{C}{K} = -\frac{u(d \ln \rho_g)/(d \ln u)}{\int_0^u du' u'^2 / [u'^\alpha (1 + u')^{3-\alpha}]}, \quad (\text{B3})$$

where $u \equiv r/R_0$. We adopt the boundary condition that at the virial radius, the slope of ICM traces that of the dark matter distribution. Then

$$\frac{C}{K} = \frac{c_{vir} [1 + (2c_{vir})/(1 + c_{vir})]}{\ln(1 + c_{vir}) - c_{vir}/(1 + c_{vir})}, \quad (\text{B4})$$

where $c_{vir} = r_{vir}/R_0$.

In the case of polytropic ICM, following Komatsu & Seljak (2001) we have

$$\frac{C}{K_0} = \frac{3}{\eta(0)} \frac{c_{vir}}{m(c_{vir})}, \quad (\text{B5})$$

where

$$m(c_{vir}) = \ln(1 + c_{vir}) - \frac{c_{vir}}{1 + c_{vir}},$$

$$s_{\star} = -\left[\alpha + (3 - \alpha)\frac{c_{vir}}{1 + c_{vir}}\right],$$

and

$$\eta(0) = \gamma^{-1}\left\{-\frac{3}{s_{\star}} + 3(\gamma - 1)\frac{c_{vir}}{m(c_{vir})}\left[1 - \frac{\ln(1 + c_{vir})}{c_{vir}}\right]\right\}.$$

REFERENCES

- Allen, S.W., Schmidt, R. W., & Fabian, A. C. 2002, MNRAS, 335, 256
- Bartelmann, M., King, L. T., & Schneider, P. 2001, A&A, 376, 361
- Binney, J. 1985, MNRAS, 212, 767
- Binney, J., & de Vaucouleurs, G. 1981, MNRAS, 194, 679
- Binney, J., & Tremaine, S. 1987, Galactic Dynamics (Princeton: Princeton Univ. Press)
- Birkinshaw, M. 1999, Physics Report, 310, 97
- Buote, D. A., & Lewis, A. D. 2004, ApJ, 604, 116
- Carlstrom, J. E., Holder, G. P., & Reese, E. D., 2002, ARA&A, 40, 643
- Cooray, A. R. 2000, MNRAS, 313, 783
- Dalal, N., Holder, G., & Hennawi, J. 2004, ApJ, in press (astro-ph/0310306)
- Dubinski, J. 1994, ApJ, 431, 617
- Fukushige, T., & Makino, J. 1997, ApJ, 477, L9
- Fukushige, T., & Makino, J. 2001, ApJ, 557, 533
- Grego, L. et al. 2004, ApJ, 608, 731
- Grego, L. et al. 2001, ApJ, 552, 2
- Holder, G. P., Mohr, J. J., Carlstrom, J. E., Evrard, A. E., & Leitch, E. M. 2000, ApJ, 544, 629
- Jenkins, A. et al. 2001, MNRAS, 321, 372
- Jing, Y. P. 2000, ApJ, 535, 30

- Jing, Y. P., Mo, H. J., Borner, G., & Fan, L. Z. 1995, MNRAS, 276, 417
- Jing, Y. P., & Suto, Y. 2000, ApJ, 529, L69
- Jing, Y. P., & Suto, Y. 2002, ApJ, 574, 538
- Komatsu, E., & Seljak, U. 2001, MNRAS, 327, 1353
- Lee, J., & Suto, Y. 2003, ApJ, 585, 151
- Lee, J., & Suto, Y. 2004, ApJ, 601, 599
- Li, Li-Xin, & Ostriker, J. P. 2002, ApJ, 566, 652
- Meneghetti, M., Bartelmann, M., & Moscardini, L. 2003, MNRAS, 340, 105,
- Meneghetti, M., Yoshida, N., Bartelman, M., Moscardini, L., Springel, V., Tormen, G., & White, S. D. M. 2001, MNRAS, 325, 435
- Mohr, J. J., Evrard, A. E., Fabricant, D. G., & Geller, M. J. 1995, ApJ, 447, 8
- Moore, B., Govemato, F., Quinn, T., Stadel, J., & Lake, G. 1998, ApJ, 499, L5
- Navarro, J. F., Frenk, C. S., & White, S. D. M. 1996, ApJ, 462, 563
- Navarro, J. F., Frenk, C. S., & White, S. D. M. 1997, ApJ, 490, 493
- Oguri, M., Lee, J., & Suto, Y. 2003, ApJ, 599, 7
- Oguri, M., & Keeton, C. 2004, ApJ, in press (astro-ph/0403633)
- Rosati, P., Borgani, S., & Norman, C. 2002, ARA&A, 40, 539
- Spergel, D. N. et al. 2003, ApJS, 148, 175
- Stark, A. 1977, ApJ, 213, 268
- Sunyaev, R. A., & Zel'dovich, Ya. B. 1970, Comments Astrops. Space Phys., 2, 66
- Sunyaev, R. A., & Zel'dovich, Ya. B. 1972, Comments Astrops. Space Phys., 4, 173
- Thomas, P. A., et al. 1998, MNRAS, 296, 1061
- Viana, P. T. P., & Liddle, A. R. 1999, MNRAS, 303, 535
- Wyithe, J. S. B., Turner, E. L., & Spergel, D. N. 2001, ApJ, 555, 504

Yoshida, N., Springel, V., White, S. D. M., & Tormen, G. 2000, ApJ, 544, L87

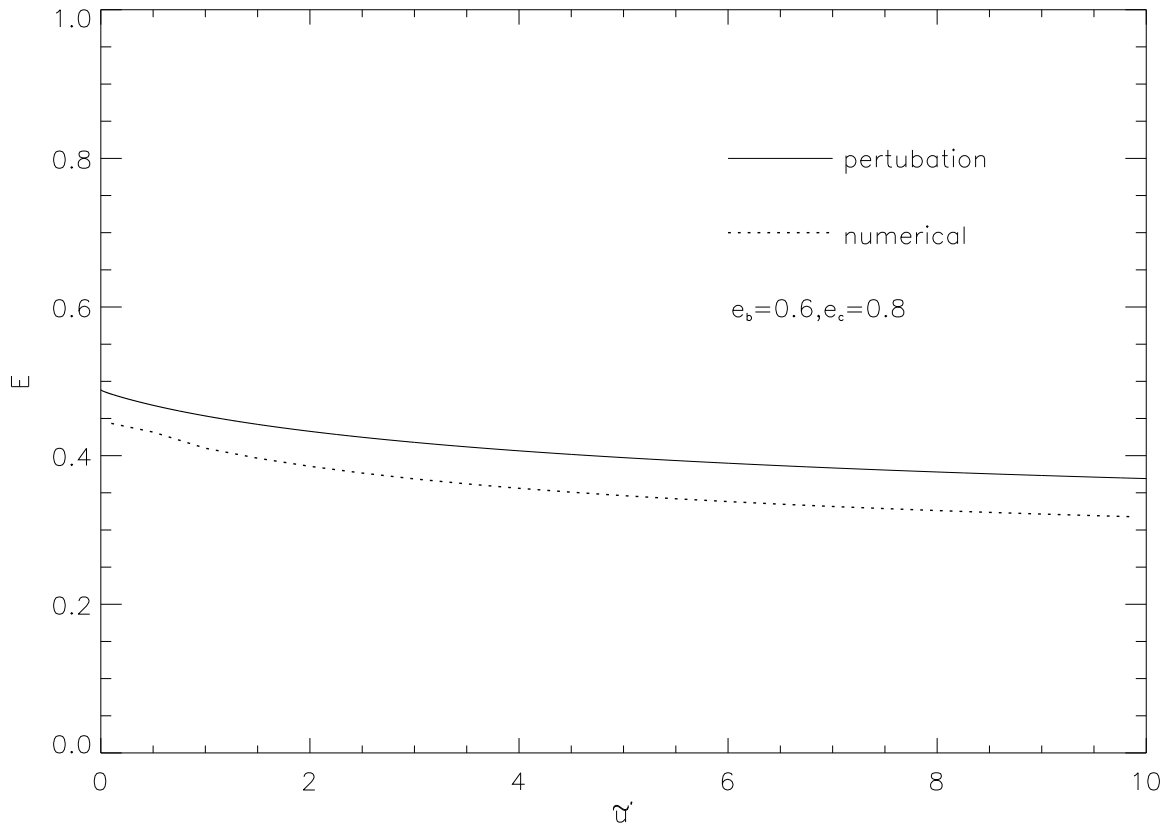


Fig. 1.— The eccentricity of isothermal SZ effect along the major axis. The cluster mass is $M = 10^{14}h^{-1}M_{\odot}$, and $e_b = 0.6$ and $e_c = 0.8$. The line-of-sight direction is $\theta = 0$ and $\phi = 0$. The solid line is the perturbative results of equation (25), and the dotted line is the results derived from numerical calculations without small e_b and e_c approximation.

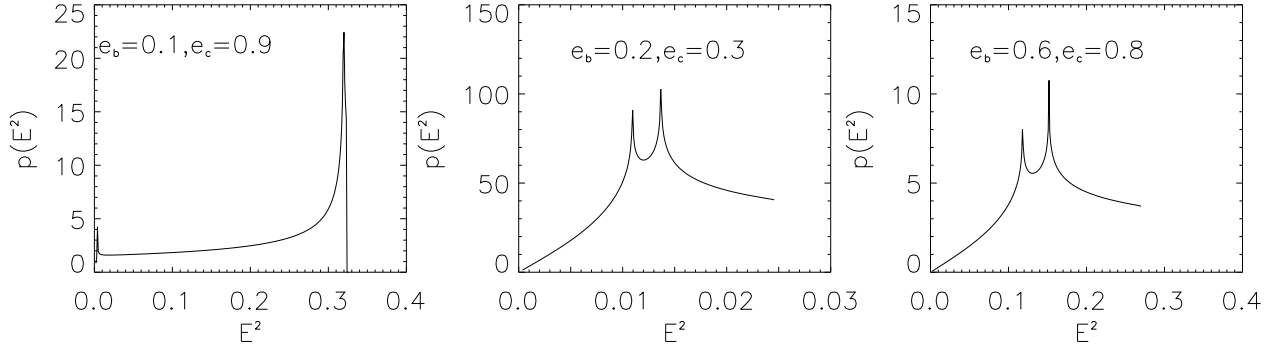


Fig. 2.— The conditional probability $p(E^2|c_e, c/b, c/a)$ for isothermal SZ effects. The mass of the cluster is $M = 10^{14}h^{-1}M_\odot$, and the redshift is $z = 0$. The eccentricity is measured at r_{vir} . Three sets of (e_b, e_c) are given. For each set, c_e is taken as the average value calculated from the fitting formula of Jing and Suto (2002).

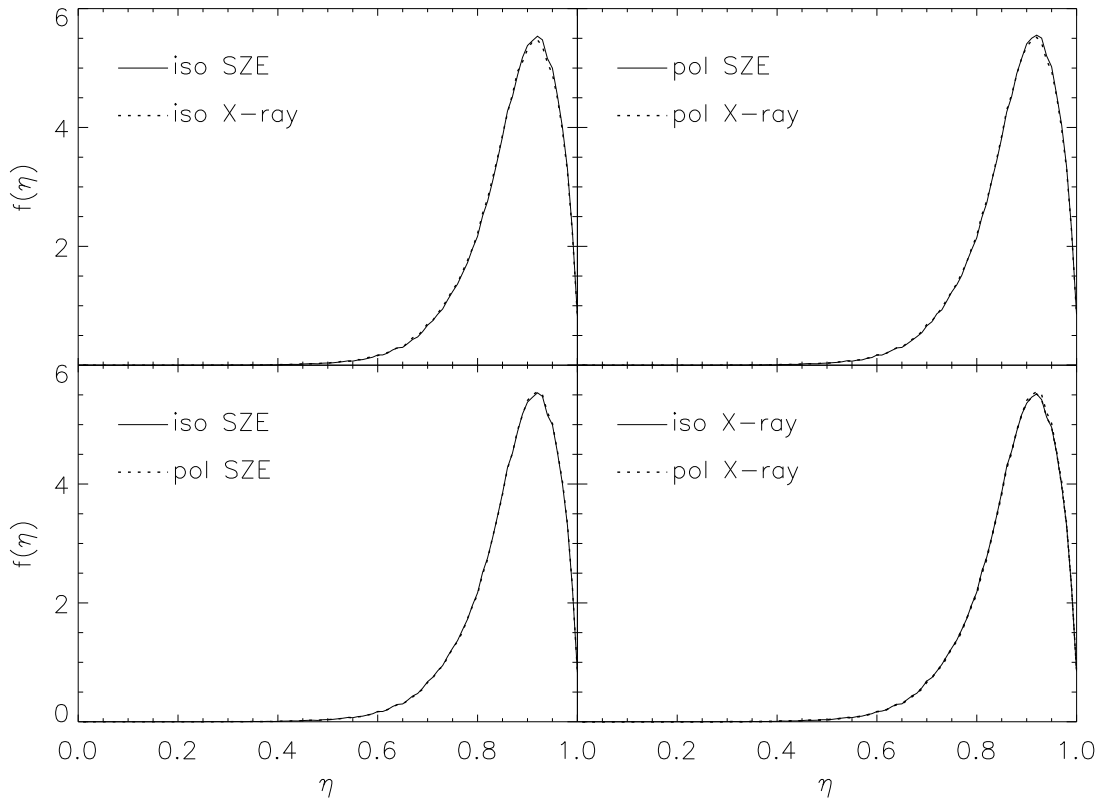


Fig. 3.— The probability function $f(\eta)$ of the axial ratio η for $M = 10^{14}h^{-1}M_{\odot}$ and $z = 0$.

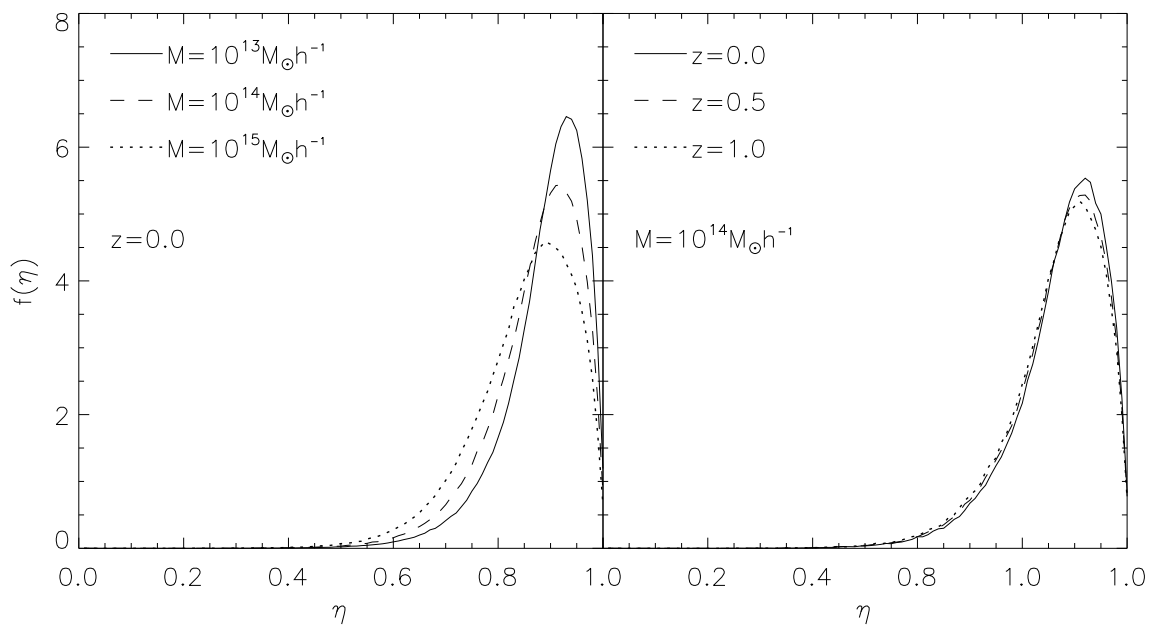


Fig. 4.— The probability function $f(\eta)$ for isothermal SZ effects. Left panel: The clusters are at $z = 0$. The solid line is for $M = 10^{13}h^{-1}M_{\odot}$. The dashed line is for $M = 10^{14}h^{-1}M_{\odot}$. The dotted line is for $M = 10^{15}h^{-1}M_{\odot}$. Right panel: $M = 10^{14}h^{-1}M_{\odot}$. The solid, dashed, and dotted lines represent results of $z = 0, 0.5$ and 1.0 , respectively.

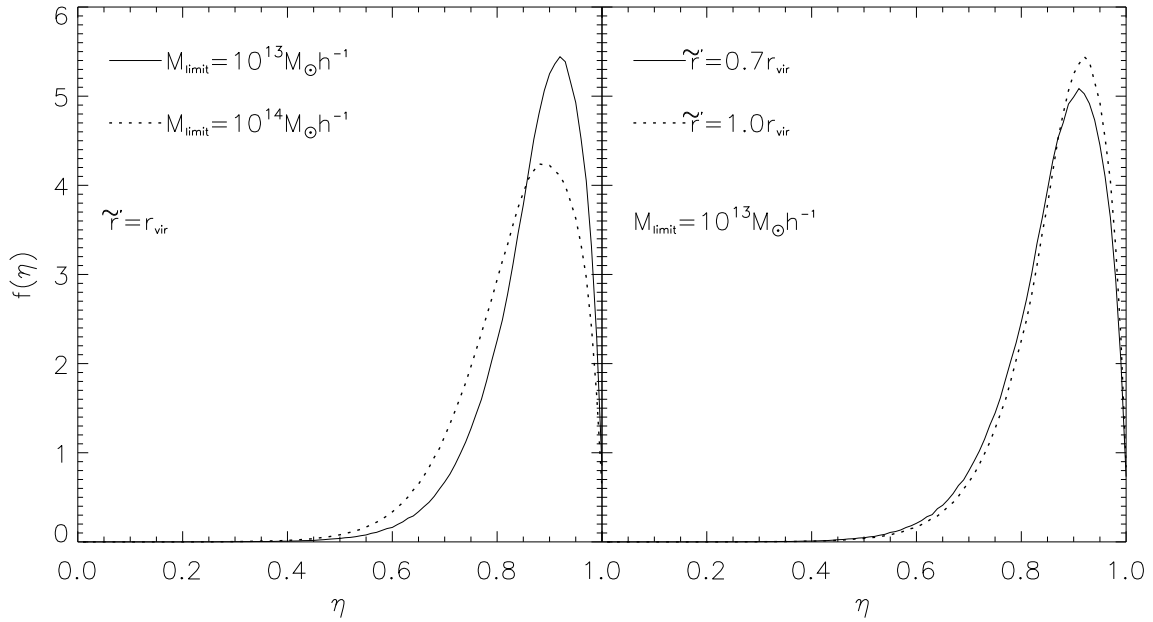


Fig. 5.— The probability function $f(\eta)$ for mass-limited cluster samples. Left panel: The solid line is for $M_{\text{lim}} = 10^{13} h^{-1} M_{\odot}$, and the dotted line is for $M_{\text{lim}} = 10^{14} h^{-1} M_{\odot}$. The axial ratio is measured at the virial radius r_{vir} . Right panel: The solid and dotted lines are for the results that η is measured at $0.7 r_{\text{vir}}$ and r_{vir} , respectively. The cluster mass $M = 10^{13} h^{-1} M_{\odot}$.

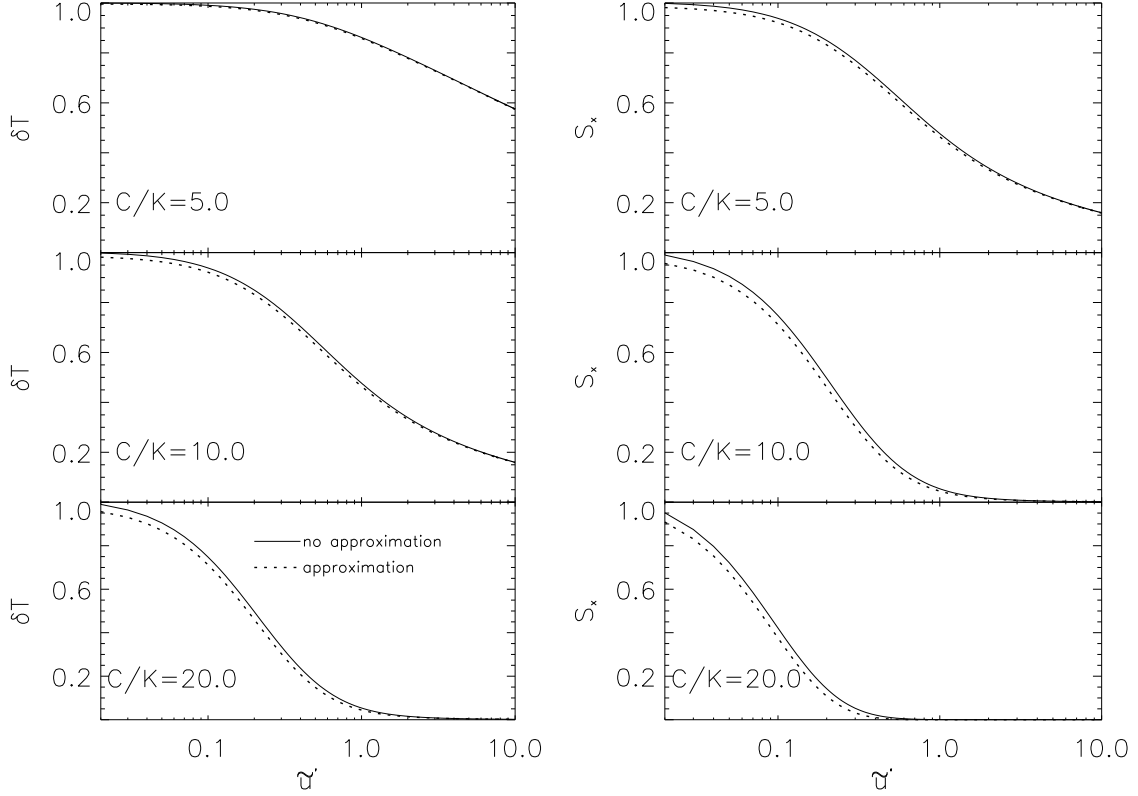


Fig. 6.— The profiles of SZ effects (left panels) and X-ray emissions (right panels) along the major axis for isothermal ICM. The cluster parameters and the line-of-sight parameters are the same as those in Figure 1. The solid line in each panel represents the results from direct integration along the line-of-sight [equation (14) for SZ effect]. The dotted line is calculated from the expansion [equation (25) for SZ effect]. The parameter $C/K = 5, 10$ and 20 , respectively.